Preparation and characterization of macroporous $Li_{1.2}Mn_{0.54}Ni_{0.13}Co_{0.13}O_2$ cathode material for lithium-ion batteries via aerogel template

S.J. Shi, J.P. Tu*, Y.Y. Tang, Y.Q. Zhang, X.L. Wang, C.D. Gu

State Key Laboratory of Silicon Materials, Key Laboratory of Advanced Materials and Applications for Batteries of Zhejiang Province and Department of Materials Science and Engineering, Zhejiang University, Hangzhou 310027, China

HIGHLIGHTS

- Macroporous $Li[Li_{0.2}Mn_{0.54}Ni_{0.13}Co_{0.13}]O_2$ is synthesized via aerogel template.
- High discharge capacity of 244.0 mA h g^{-1} is obtained at 1 C for LMNCO-800.
- For LMNCO-900, 220.2 mA h g^{-1} is obtained at 1 C with enhanced cycle stability.
- Capacity of 129.8 mA h g^{-1} is obtained at 10 C without any fading after 120 cycles.

ARTICLE INFO

ABSTRACT

Macroporous $Li_{1.2}Mn_{0.54}Ni_{0.13}Co_{0.13}O_2$ cathode materials with high crystallinity and hexagonal ordering are synthesized by aerogel template followed by solid state reaction. High discharge capacities of 244.0 mA h g^{-1} and 153.9 mA h g^{-1} are obtained for the Li-rich layered oxide synthesized at 800 °C at current densities of 200 mA g^{-1} and 2000 mA g^{-1} between 2.0 V and 4.8 V. Increasing the synthesis temperature to 900 °C, the macroporous $Li_{1.2}Mn_{0.54}Ni_{0.13}Co_{0.13}O_2$ delivers a high discharge capacity of 220.2 mA h g^{-1} at a current density of 200 mA g^{-1} with a capacity retention of 89.1% after 50 cycles, 129.8 mA h g^{-1} at a current density of 2000 mA g^{-1} and almost no capacity fading after 120 cycles. The diffusion coefficients of Li^+ in the Li-rich layered oxide determined by galvanostatic intermittent titration technique are in the range of 5.0×10^{-18}–8.0×10^{-14} cm^2 s^{-1}. Electrochemical impedance spectroscopy indicates that the macroporous structure with good particle contact of the layered oxide can improve its rate capability and cyclic stability.

© 2013 Elsevier B.V. All rights reserved.

1. Introduction

Next-generation lithium-ion batteries are critically dependant on finding a new lithium-intercalation cathode material that can store more energy and deliver it at high power, whilst being safer and cheaper, which is essential for applications in electric vehicles and hybrid vehicles, and so forth. $LiNi_{1/3}Co_{1/3}Mn_{1/3}O_2$ which integrates the features of $LiCoO_2$, $LiNiO_2$ and $LiMnO_2$ has already been widely investigated to replace $LiCoO_2$ due to its favorable benefits such as high capacity, structural stability, low cost and safety [1–7]. Recently, it has been shown that the addition of extra lithium, manganese, and charge-compensating oxygen into $LiMn_{1/3}Ni_{1/3}Co_{1/3}O_2$ results in the formation of Li_2MnO_3-like regions to stabilize the electrode structure and enhance the discharge capacity by extracting the lithium concomitant with release of oxygen (a net loss of Li_2O), typically at 4.6–4.8 V, to form a layered MnO_2 component [8–15]. As reported, the $Li[Li_{0.2}Mn_{0.54}Ni_{0.13}Co_{0.13}]O_2$ cathode material, which is also rewritten in two-component notation as $0.5Li_2MnO_3 \cdot 0.5LiNi_{1/3}Co_{1/3}Mn_{1/3}O_2$, can deliver an initial discharge capacity as high as 250 mA h g^{-1} between 4.8 and 2.0 V at room temperature [16–22].

To explore the capability of Li-rich manganese nickel cobalt oxides as a new cathode material in lithium-ion batteries, many methods have been recently developed to prepare high quality Li-rich manganese nickel cobalt oxides, such as co-precipitation [17,23–25], microwave heating process [26], sol–gel [10,27,28], ion–exchange reaction [29] and solid reaction [30]. The nanostructured $Li[Li_{0.2}Mn_{0.54}Ni_{0.13}Co_{0.13}]O_2$ materials have been widely achieved to deliver high discharge capacity due to the more active surface available. However, with greater percentage of nanoparticles, undesirable reactions with the electrolyte would happen

on the particle surface during charge–discharge processes to form the solid electrolyte interphase (SEI) layer, which might result in high fade rates as the active particles were coated and electronically isolated [10,20].

An alternative approach to particle morphology design is to incorporate micrometer porosity into particles. Good particle–particle contacts are maintained to maximize the rate capability benefits and improve the cyclic stability [31,32]. Such strategy has been applied to prepare macroporous $LiNi_{1/3}Co_{1/3}Mn_{1/3}O_2$ cathode materials with liquid phase precursor [33], triblock copolymer template [34] and carbon sphere template method [35]. In addition, aerogel template has been used to prepare porous material such as carbon [36,37], V_2O_5 [38,39] to obtain high specific capacity. In this present work, agar is used to form aerogel as template to prepare macroporous $Li[Li_{0.2}Mn_{0.54}Ni_{0.13}Co_{0.13}]O_2$. Such method is simple to approach satisfactory rate capability and cyclic stability of Li-rich layered oxide cathode materials.

2. Experimental

To prepare aerogel, 1.5 g agar was added into 100 ml de-ionized water and heated in an oil bath pan to reach 95 °C. The agar will be dissolved in the de-ionized to form a transparent solution with fierce stirring. Stoichiometric amounts of $LiNO_3$, $Ni(NO_3)_2\cdots 6H_2O$, $Co(NO_3)_2\cdots 4H_2O$ and $Mn(NO_3)_2\cdots 4H_2O$ were added in the resulting agar solution. After stirring for 1 h at 95 °C, a red transparent solution is obtained. The total concentration of nitrate is 0.5 M. The solution was pulled into a culture dish and a transparent gel formed when the solution was cooled to room temperature. Then the as-confected gel was freeze-dried at −20 °C for more than 2 days until the gel became an aerogel. The aerogel was first calcined at 500 °C for 2 h in air to remove the organic component in a chamber furnace. And then, the obtained powder was ground and again calcined at 700 °C, 800 °C and 900 °C in air for 16 h to get Li-rich layered oxide $Li[Li_{0.2}Mn_{0.54}Ni_{0.13}Co_{0.13}]O_2$. The as-synthesized oxides were named as LMNCO-700, LMNCO-800 and LMNCO-900 for short. Furthermore, another powder synthesized at 800 °C through the same way without agar was performed as a contrast. The oxide was named as C-LMNCO-800 for short.

The morphologies and structures of the as-synthesized powders were characterized using field emission scanning electron microscopy (FESEM, S-4800 coupled with EDX) and transmission electron microscopy (TEM, Tecnai G2 F30 S-Twin). X-ray diffraction (XRD) measurements were collected on a Rigaku D/Max-2550pc X-Ray diffractometer, using CuKα radiation at 40 kV and 250 mA from 2θ degree of $10.0°–80.0°$, with an increasing step of 0.02° and counting time duration of 1.0 s for each step. The specific surface areas of the powders were measured following the multipoint Brunauer–Emmett–Teller (BET) procedure from the N_2 adsorption–desorption isotherms using an AUTOSORB-1-C gas sorption analyzer.

The working electrodes were prepared by a slurry coating procedure. The slurry consisted of 85 wt.% as-synthesized materials, 10 wt.% carbon conductive agent (acetylene black) and 5 wt.% polyvinylidene fluoride (PVDF) was coated on aluminum foil. After drying at 90 °C for 24 h in vacuum, the sample was pressed under a pressure of 20 MPa. A metallic lithium foil served as the anode, 1 M $LiPF_6$ in ethylene carbonate (EC)-dimethyl carbonate (DMC) (1:1 in volume) was used as the electrolyte, and a polypropylene microporous film (Cellgard 2300) as the separator. The cells were assembled in an argon-filled glove box with H_2O concentration below 1 ppm. The galvanostatic charge–discharge tests were performed with coin-type cells (CR2025) on a LAND battery program-control test system (Wuhan, China) between 2.0 and 4.8 V at the charge–discharge densities from 20 to 2000 mA g^{-1} at room temperature. Galvanostatic intermittent titration technique (GITT) was also conducted on this apparatus at room temperature in the voltage range of 2.0–4.8 V. Cyclic voltammetry (CV) tests were carried out on an electrochemical workstation (CHI660C) in the potential window of 2.0–5.0 V (vs. Li/Li$^+$) at a scan rate of 0.1 mV s^{-1}. Electrochemical impedance spectroscopy (EIS) measurements were performed on this apparatus using a three-electrode cell with the layered oxide as the working electrode, metallic lithium foil as both the counter and reference electrodes. The amplitude of the AC signal was 5 mV over a frequency range from 100 kHz to 10 mHz at different charge states.

3. Results and discussion

3.1. Material characterization

Fig. 1 shows the XRD patterns of the Li-rich oxide powders synthesized at different temperatures. Except the superlattice peaks between 20° and 25° (in the red dashed), the other peaks can be indexed the α-NaFeO$_2$ structure with space group R-3m in these patterns. However, the splitting (006)/(102) and (108)/(110) peaks of LMNCO-700 are not distinct, indicating that the layered structure of LMNCO-700 is not well formed due to low calcination temperature of 700 °C. Contrarily, LMNCO-800 and LMNCO-900 have distinct splitting of (006)/(102) and (108)/(110) peak which indicates well-formed layered structure especially LMNCO-900. The weak peaks between 20° and 25° for the calcined products, as clearly shown in the right of Fig. 1, are consistent with the LiMn$_6$ cation arrangement that occurs in the transition metal layers of Li$_2$MnO$_3$ nano-domains, which can be indexed to the monoclinic unit cell C2/m [40,41]. No peak for any impurity phase is detected in these patterns, indicating high purity of the oxides. In addition, as the calcination temperature increases, the weak peaks with respect to the LiMn$_6$ cation arrangement become more symmetrical and sharper. It has been reported that the ordering of the oxide structure can also be indicated from the XRD patterns with the I_{003}/I_{104} and $(I_{006} + I_{012})/I_{101}$ intensity ratios. The former is reported as an index of the disorder between Li-ions and Ni-ions [42]. The latter is also called R factor $(R = (I_{006} + I_{012})/I_{101})$ [43,44]. The lower the value of R-factor is, the higher the hexagonal ordering is. The I_{003}/I_{104} ratios of LMNCO-800 and LMNCO-900 are 2.314 and 2.199, much larger than that of LMNCO-700 (1.112), indicating less disorder between Li$^+$ and Ni^{2+}. Likewise, the values of R factor are 0.250 and 0.251 for LMNCO-800 and LMNCO-900, respectively, lower than that of LMNCO-700 (0.318), indicating higher hexagonal
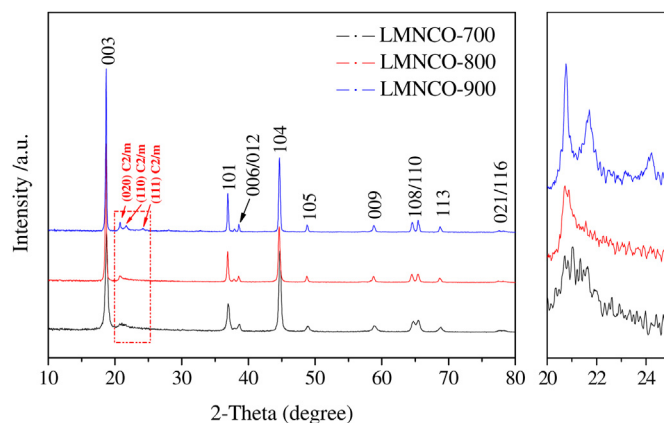

Fig. 1. XRD patterns of $Li[Li_{0.2}Mn_{0.54}Ni_{0.13}Co_{0.13}]O_2$ powders synthesized at different temperatures. The right part is the magnification of the XRD patterns from 2θ degree of $20°–25°$ in the red dashed.

ordering for LMNCO-800 and LMNCO-900. It indicates that the well-formed layered structure can be obtained only at the calcination temperatures higher than 700 °C.

Fig. 2 shows the SEM morphologies of the Li-rich layered oxides. After calcination at 500 °C, the product presents a disordered macroporous morphology which is composed of individual particles with narrow size distribution, in the range of 10–30 nm, fused together to form agglomerates with 1–5 μm in sizes (Fig. 2a). After further calcination at higher temperatures, the macroporous structure of agglomerates is still maintained. However, the primal individual particle grows large with sizes of 50–100 nm, 100–200 nm and 400–600 nm for LMNCO-700, LMNCO-800 and LMNCO-900, respectively. The use of the agar solution provides good mixing of the constituent ions at the atomic scale, while the freeze drying process retains the good mixing only with water removal. Both the removals of water and organic component result in the formation of macroporous structure after sintering, as shown in Fig. 2a–d. The oxide synthesized without agar as a contrast, no microspore is observed (Fig. 2e). The Brunauer–Emmett–Teller (BET) surface area values are 6.52, 4.57 and 2.30 m^2 g^{-1} for LMNCO-700, LMNCO-800 and LMNCO-900, respectively. Thus, there is a threefold decrease in specific surface area of the oxide powder by increasing the calcination temperature from 700 to 900 °C.

Fig. 3 shows the TEM images of LMNCO-800 and LMNCO-900 which own well-formed layered structure. Spongy morphology and irregularly agglomerated particles are obtained, as shown in Fig. 3a and c. The particle sizes are accordant with those observed in the SEM images, 100–200 nm and 400–600 nm for LMNCO-800 and LMNCO-900, respectively. Distinct lattice fringes are observed in the insert of Fig. 3b and d, indicating high crystallinity after the high temperature calcination. The lattice fringes are 4.755 Å and 4.773 Å for LMNCO-800 and LMNCO-900, respectively, which corresponds to the (003) planes [34]. It is concluded that after calcination at 800 °C and 900 °C, macroporous Li[$Li_{0.2}Mn_{0.54}Ni_{0.13}Co_{0.13}$]$O_2$ with high crystallinity can be obtained by the aerogel template.

Nitrogen adsorption/desorption isotherms and the BJH curves recorded for Li[$Li_{0.2}Mn_{0.54}Ni_{0.13}Co_{0.13}$]$O_2$ powders synthesized at 800 °C with and without aerogel template are shown in Fig. 4. It reveals clearly that when the aerogel template is performed, the pore volume is much larger than that synthesized without aerogel. The formation of hysteresis at high p/p_0 range of adsorption/desorption isotherms, which appears clearly for LMNCO-800 is due to capillary condensation, is an indication of the existence of porosity in the particles of the sample. For LMNCO-800, the BJH curve consists of two peaks. One is at about 20 nm which may be the pore between the particles. The other is from about 100 nm to 2 μm. Although, there is also a BJH peak at about 20 nm for C-
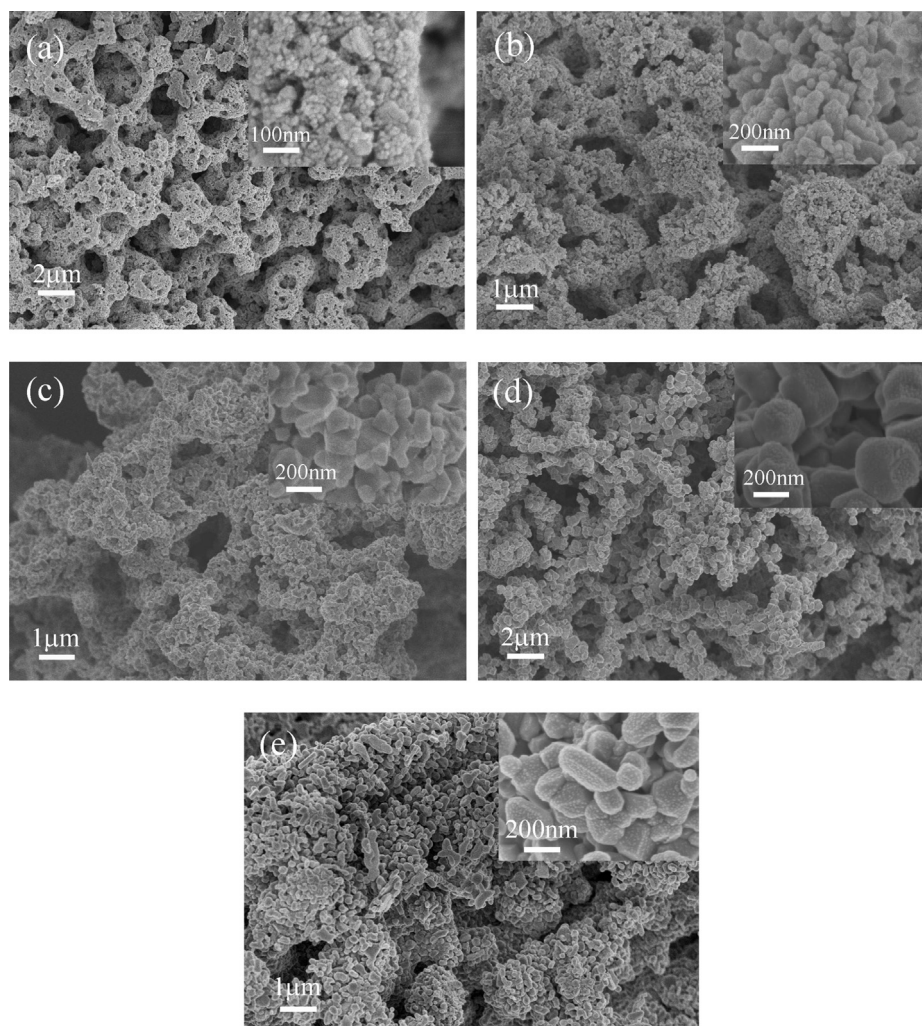

Fig. 2. SEM images of Li[$Li_{0.2}Mn_{0.54}Ni_{0.13}Co_{0.13}$]$O_2$ powders synthesized at different temperatures: (a) 500 °C, (b) 700 °C, (c) 800 °C and (d) 900 °C by aerogel template. (e) SEM images of Li[$Li_{0.2}Mn_{0.54}Ni_{0.13}Co_{0.13}$]$O_2$ powder synthesized at 800 °C without aerogel.
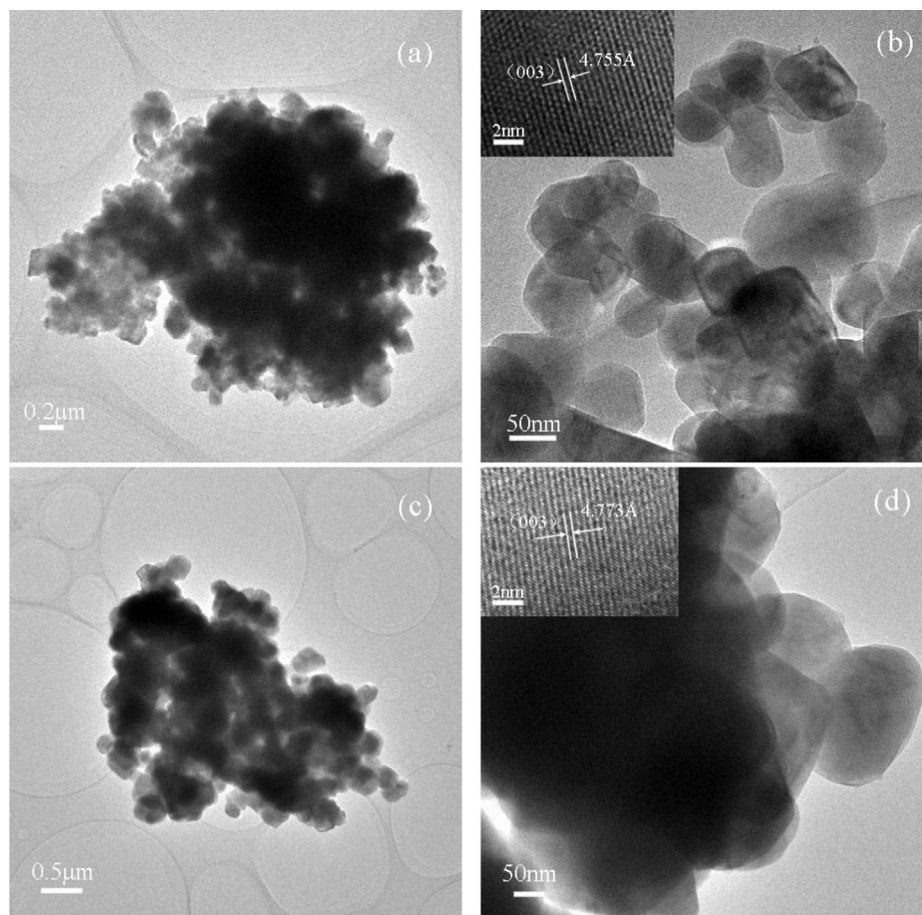
Fig. 3. TEM images of Li[Li$_{0.2}$Mn$_{0.54}$Ni$_{0.13}$Co$_{0.13}$]O$_2$ powders synthesized at (a, b) 800 °C and (c, d) 900 °C by aerogel template.

LMNCO-800, it is much weaker. And no distinct peak appears above 100 nm. That indicates that macroporous morphology can only be obtained when the aerogel template is performed. The results obtained here are accordant with those observed at SEM and TEM images.
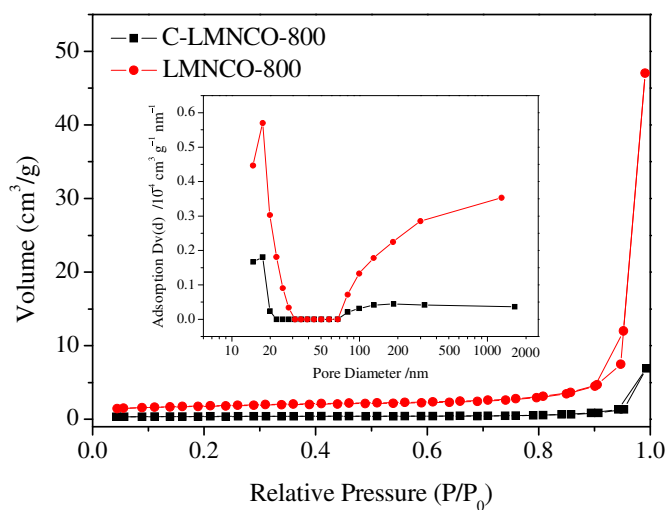

Fig. 4. Nitrogen adsorption–desorption isotherms of Li[Li$_{0.2}$Mn$_{0.54}$Ni$_{0.13}$Co$_{0.13}$]O$_2$ powders synthesized at 800 °C with and without aerogel template; the insert is the pore size distribution.

3.2. Electrochemical properties

Fig. 5a–b shows the charge–discharge curves of macroporous Li [Li$_{0.2}$Mn$_{0.54}$Ni$_{0.13}$Co$_{0.13}$]O$_2$ at a current density of 20 mA g^{-1} in the voltage range of 2.0–4.8 V for the initial and second cycles. Noting from Fig. 5a, as normal Li-rich layered oxides, there are two charge platforms in the initial cycle, one at 4.0 V and the other at about 4.5 V. The first one is the Li-extraction from the structure of space group R-3m accompanying with the oxidation of mainly Ni^{2+}/Ni^{4+} and partly Co^{3+}/Co^{4+} at about 4.0 V. The other at 4.5 V represents the activation of the Li$_2$MnO$_3$-like region which appears only in the initial cycle. As shown in Fig. 5b, the charge platform at 4.5 V disappears in the second cycle due to the irreversible activation. The initial charge and discharge capacities are 344.9/255.2 mA h g^{-1}, 359.3/287.5 mA h g^{-1} and 365.2/262.8 mA h g^{-1} for LMNCO-700, LMNCO-800 and LMNCO-900, respectively. The charge capacities approach to the theoretical value (377.1 mA h g^{-1}, calculated from the parent Li[Li$_{0.2}$Mn$_{0.54}$Ni$_{0.13}$Co$_{0.13}$]O$_2$). However, the initial coulombic efficiency is low, only 70%–80.0% for all the Li-rich oxide electrodes, large capacity is lost during the initial cycle. The lost capacity is ascribed to the irreversible removal of Li$_2$O from the Li$_2$MnO$_3$ region, the degradation of electrolyte and the formation of SEI film. Among them, the removal of Li$_2$O from the Li$_2$MnO$_3$ region is the main reason for the low initial coulombic efficiency due to its irreversibility [45,46]. The electrochemical inactive Li$_2$MnO$_3$ region becomes active after removing of Li$_2$O from the lattice during the activation process at about 4.5 V. And about all the Li ions can reinsert into the layered structure after activation, which is

(a)

(b)
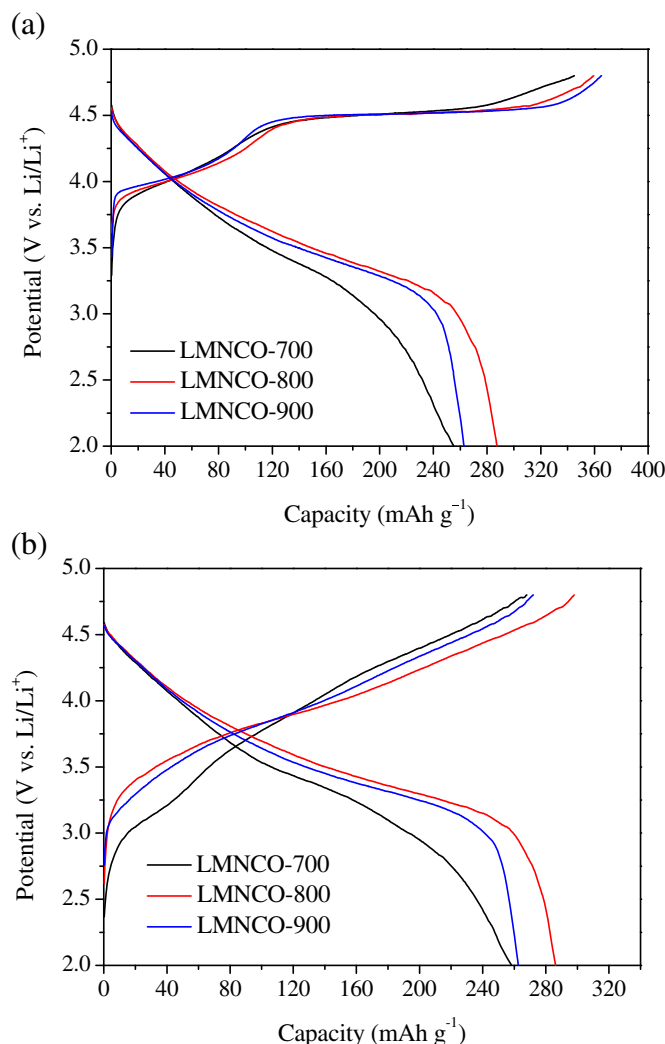
Fig. 5. Initial (a) and second (b) charge–discharge curves of macroporous Li [Li$_{0.2}$Mn$_{0.54}$Ni$_{0.13}$Co$_{0.13}$]O$_2$ at a current density of 20 mA g^{-1} in the voltage range of 2.0–4.8 V.

different from the normal layered oxides such as LiMn$_{1/3}$Ni$_{1/3}$Co$_{1/3}$O$_2$ [47]. For LMNCO-800, the initial discharge capacity even surpasses the theoretic value (276 mA h g^{-1}, calculated from LiMO$_2$, M = Mn, Co, Ni, after activation). It is reported that anomalously high capacity above the theoretically expected value can be obtained from Li[Li$_{0.2}$Mn$_{0.54}$Ni$_{0.13}$Co$_{0.13}$]O$_2$ [20,47]. Although the origin of the exceptionally high capacity is not yet known, it has been speculated that the anomalous capacity is ascribed to oxygen ion vacancies, which are produced owing to the removing of Li$_2$O during the first cycle. The as-produced oxygen ion vacancies which were partly maintained temporarily could accommodate the Li$^+$ during the following discharge process, leading to the anomalous capacity for the initial cycle [20,47].

Fig. 6 shows the cycle performance of the macroporous Li-rich oxide electrodes at a current density of 200 mA g^{-1}. It clearly reveals that LMNCO-800 has a high initial discharge capacity of 233.6 mA h g^{-1} and reaches the maximum of 244.0 mA h g^{-1} after several cycles. LMNCO-900 also delivers a high initial discharge capacity of 201.7 mA h g^{-1} and the maximum of 220.2 mA h g^{-1} due to its perfect layered structure though it has Contrarily specific surface area comparing to LMNCO-800. LMNCO-700 which has unsatisfactory layered structure has the least discharge capacity with a maximum of 201.2 mA h g^{-1}. In contrast, the initial
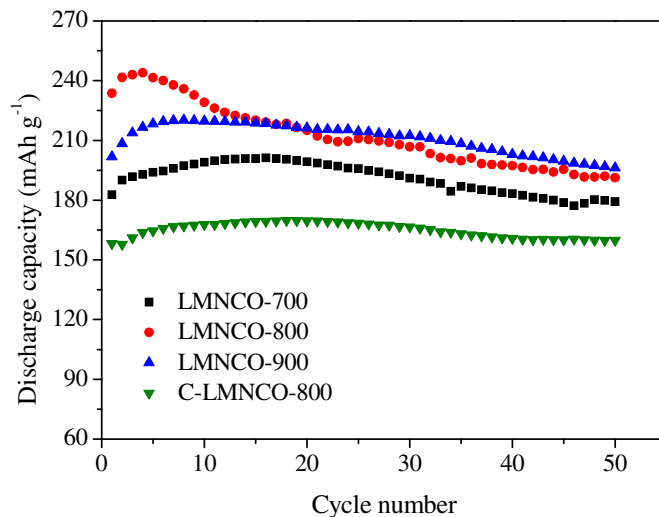
Fig. 6. Cycle performances of macroporous Li[Li$_{0.2}$Mn$_{0.54}$Ni$_{0.13}$Co$_{0.13}$]O$_2$ at a current density of 200 mA g^{-1}.

discharge capacity of C-LMNCO-800, which is synthesized without the aerogel template, is only 158.3 mA h g^{-1}. There is not any dispersant such as chelating agent used in the synthesis processes for the comparing experiment. The transition metal ions may not always be dispersed well during the whole synthesis process. Furthermore, macroporous morphology with good contacts between active particles is not obtained here. LMNCO-900 has much higher discharge capacity than the Li-rich oxides prepared by some other methods [16,18,19] in despite of its submicron particulate. However, LMNCO-800 which has the highest discharge capacity displays low capacity retention of 78.4% after 50 cycles with capacity retained of 191.3 mA h g^{-1}. To our satisfactory, LMNCO-900 which can also deliver high discharge capacity, has a high capacity retention of 89.1% (corresponding to the maximum) after 50 cycles.

Two main factors have been demonstrated to affect the cycle stability of Li-rich layered oxides [48–51]. One is the dissolution of the metal ions, especially the manganese ion during the charge–discharge process. The mechanism of the Mn dissolution can be explained as follows:

$$Mn^{3+} \xrightarrow{charge-discharge} Mn^{4+} + Mn^{2+} \tag{1}$$
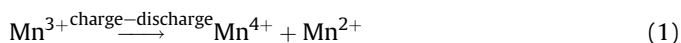
Not all the Mn ions are in the oxidation state of 4+, part will stay at the oxidation state of 3+ after high temperature treatment, and this part of Mn will easily be dissolved. In addition, during discharging to a low potential, part of Mn^{4+} will be reduced to Mn^{3+}. The dissolution will seriously destroy the oxide surface and an unsatisfactory SEI film will form. This may be the reason for the low capacity retention of LMNCO-800 due to the large specific surface area. The other is the Jahn–Teller distortion during the cycling process. If Li[Li$_{0.2}$Mn$_{0.54}$Ni$_{0.13}$Co$_{0.13}$]O$_2$ completely delithiated during charge, then it would yield Mn$_{0.675}$Ni$_{0.1625}$Co$_{0.1625}$O$_2$ in which the manganese ions were tetravalent, higher than that expected for a potentially damaging Jahn–Teller distortion [46].

Fig. 7a shows the rate capability of macroporous Li[Li$_{0.2}$Mn$_{0.54}$Ni$_{0.13}$Co$_{0.13}$]O$_2$ from current density of 20–2000 mA g^{-1} between 2.0 V and 4.8 V at room temperature. The cells were charged and discharged at the same current density. LMNCO-800 has the best rate capability among these oxides, and the discharge capacities of 284.2, 230.8, 221.2, 207.4, 192.0, 170.4 and 150.4 mA h g^{-1} are

(a)

(b)
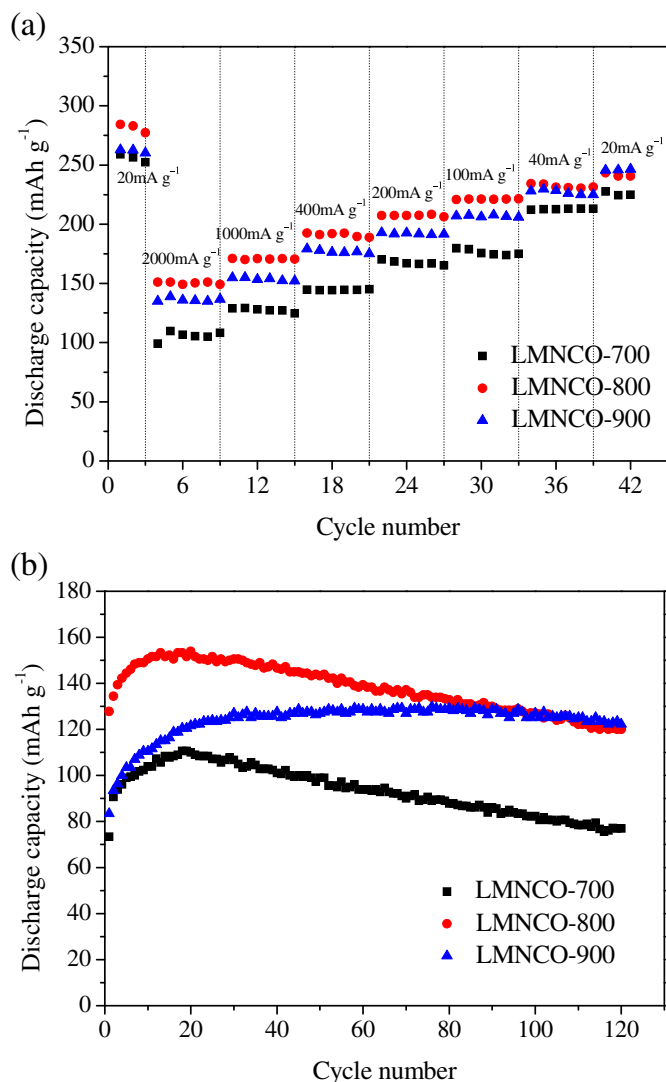
**Fig. 7.** (a) Rate capability of macroporous $Li[Li_{0.2}Mn_{0.54}Ni_{0.13}Co_{0.13}]O_2$, the cells were charged and discharged at the same current densities, (b) cycle performances performed at a current density of 2000 mA g^{-1}.

obtained at current densities of 20, 40, 100, 200, 400, 1000 and 2000 mA g^{-1}, respectively. The rate capability is much higher than that of the pristine materials prepared by other methods [10,16,19]. It is partly attributed to the well-formed layered structure. Furthermore, small particle size, good contacts between the active particles and macro porosity also contribute a lot. LMNCO-900 which has much larger particle size also exhibits satisfactory rate capability due to the merit of macroporous structure. It delivers discharge capacities of 262.8, 228.4, 207.7, 192.8, 179.1, 153.9 and 135.5 mA h g^{-1} at current densities of 20, 40, 100, 200, 400, 1000 and 2000 mA g^{-1}, respectively. However, LMNCO-700 without perfect layered structure exhibits the worst rate capability. Furthermore, it seems that the intrinsic conductivity of Li-rich layered oxide is poor, and the transformation from $xLi_2MnO_3(1-x)LiMO_2$ to Li_xMO_2 (M = Mn, Co, Ni) will disorder the well-formed crystal lattice, leading to low Li$^+$ diffusion, which is accordant with the result of GITT later. Thus, the effect of particle size, contacts between the active particles and the as-formed macroporous structure are much more important for the rate capability. The posterior two factors may partly compensate the first one, resulting in improved rate capability of LMNCO-900.

The cycle performance performed at a current density of 2000 mA g^{-1} is shown in Fig. 7b. At such high current density, a long activation appears for 20 to 40 cycles before the maximum of discharge capacity of the electrodes is achieved. The maximal discharge capacities are 110.6, 153.9 and 129.8 mA h g^{-1} for LMNCO-700, LMNCO-800 and LMNCO-900, respectively. A discharge capacity of 122.2 mA h g^{-1} is retained for LMNCO-900 after 120 cycles, revealing its excellent cyclic stability. Good contacts between the active particles and the as-formed macroporous structure contribute a lot to the capacity achievement of LMNCO-900 at high current densities, in despite of its large particle size and small specific surface area.
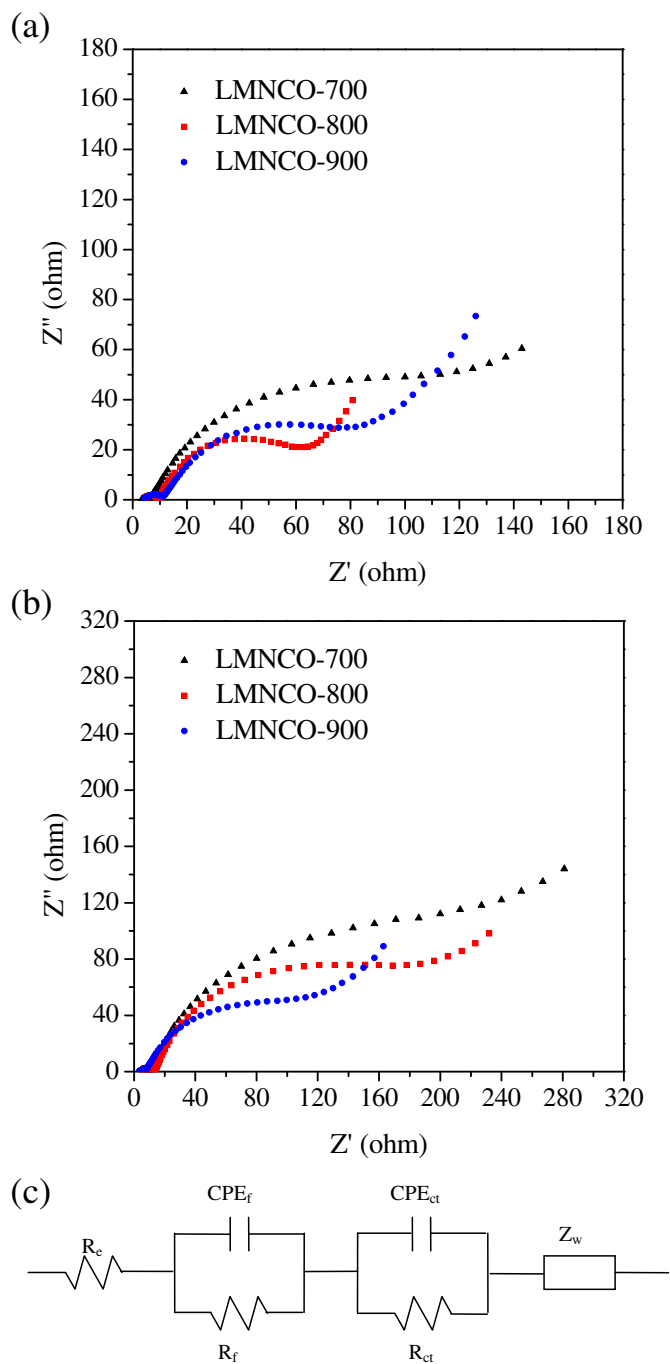
CV tests were performed to further understand the oxides synthesized by aerogel template. Fig. 8a–c shows the CV curves of macroporous $Li[Li_{0.2}Mn_{0.54}Ni_{0.13}Co_{0.13}]O_2$ synthesized at different temperatures for the initial two cycles. The initial CV curve for the oxidation section of LMNCO-800 and LMNCO-900 are sharp and symmetrical. There are two main anodic peaks, one at about 3.9 V and another at about 4.6 V (vs. Li/Li$^+$). The peak at the low potential is ascribed to the extraction of Li$^+$ from the $LiMO_2$ (M = Mn, Ni, Co) structure. And another peak at 4.6 V is associated with the activation of the Li_2MnO_3 region, extraction of Li$^+$ from $Li[Li_{1/3}Mn_{2/3}]O_2$. It has been demonstrated that when the Li_2MnO_3-based material is charged above 4.4 V, the excess Li will extract from the Li_2MnO_3 region, accompanying with loss of O [46]. Interestingly, the inactive $Li[Li_{1/3}Mn_{2/3}]O_2$ becomes active [MnO_2], and during the following discharge process, a high initial discharge capacity of 287.5 mA h g^{-1} is obtained for LMNCO-800 at a current density of 20 mA g^{-1}, exceeding the theory capacity. However, in the second cycle, the activation peak disappears and a broad peak appears at 3.85 V which is the main anodic peak for the newly formed $Li[M]O_2$ (M = Mn, Ni, Co) (Supposing that after initial activation all the Li is removed from $Li[Li_{0.2}Mn_{0.54}Ni_{0.13}Co_{0.13}]O_2$. Thus, $[MO_2]$ (M = Mn, Ni, Co) forms and if Li is re-inserted, $Li[M]O_2$ (M = Mn, Ni, Co) is obtained). Two cathodic peaks are evident during the discharge process. Although it is impossible to differentiate the reduction processes of the individual Mn, Ni and Co from the data, it is believed from the theoretical studies that the process at about 4.5 V may be associated with the occupation of tetrahedral sites by lithium within the extensively delithiated layer and the low potential processed at ∼3.25 V corresponds to the occupation of octahedral sites, in agreement with the reports of Hayley et al. [52]. However, because of the faulty layered structure, the CV curves of LMNCO-700 are broad, less symmetrical, and the intensities of the anodic and cathodic peaks are much lower than those of LMNCO-800 and LMNCO-900. It is accordant with the electrochemical performances obtained former.

EIS tests were performed after cycling at a current density of 200 mA h g^{-1} for 3 cycles and 50 cycles. Fig. 9a and b shows the Nyquist plots of Li-rich layered electrodes at the charge state of 4.5 V after 3 and 50 cycles, respectively. The shapes of all the Nyquist plots are similar. They are composed of a small interrupt and a semicircle in the high frequency, a semicircle in the high to medium frequency and a quasi-straight line in the low frequency. The small interrupt in the high frequency which corresponds to the solution impedance R_e, is almost the same for all the oxide electrodes. The small semicircle in the high frequency is assigned to the impedance (R_f) of Li$^+$ diffusion in the surface layer (SEI film); another semicircle in the high to medium frequency indicates the charge transfer impedance (R_{ct}), relating to charge transfer through the electrode/electrolyte interface. And the quasi-straight line in the low frequency represents the Warburg impedance, which is related to the solid-state diffusion of Li$^+$ in the electrode materials [18,53]. In order to further understand the Nyquist plots, an equivalent circuit is used to fit them, as shown in Fig. 9c. CEP_f, CEP_{ct}
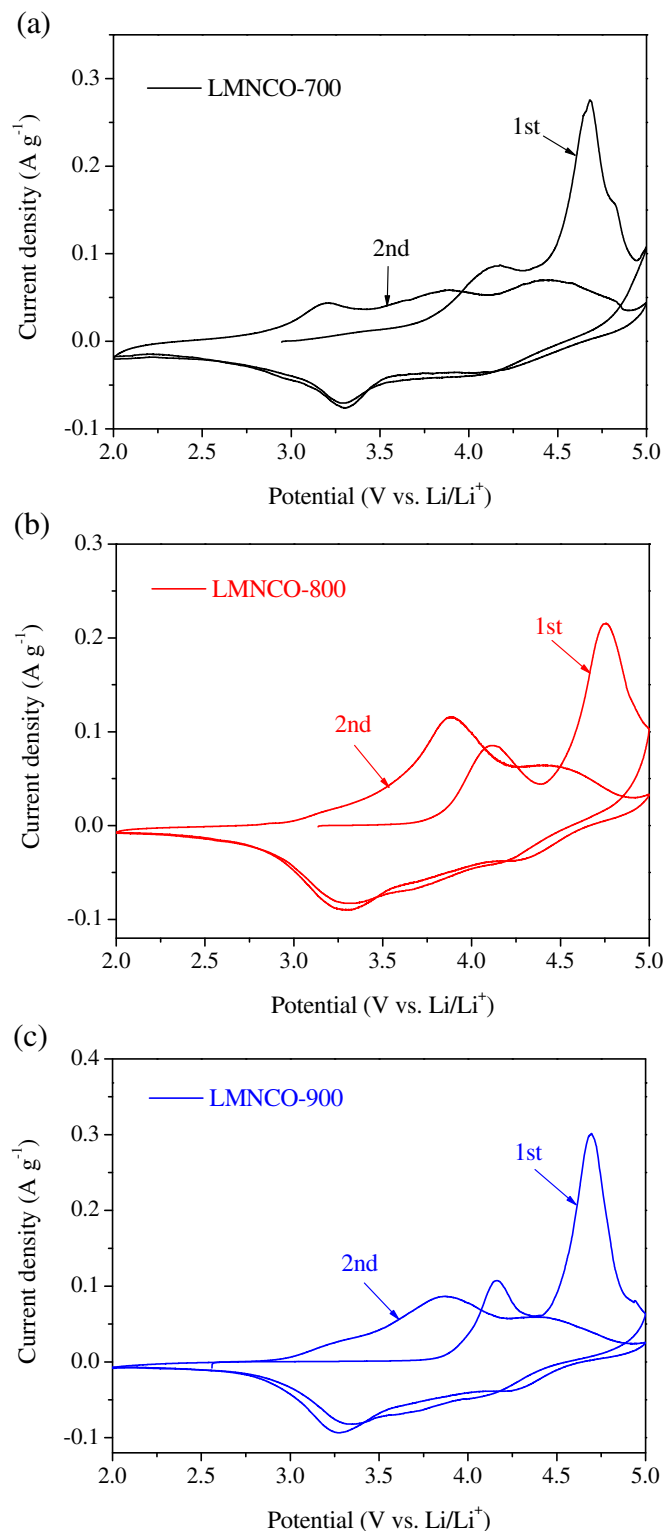
Fig. 8. CV curves of macroporous Li[Li$_{0.2}$Mn$_{0.54}$Ni$_{0.13}$Co$_{0.13}$]O$_2$ for the initial two cycles in the potential range of 2.0–5.0 V (vs. Li/Li$^+$) at a scan rate of 0.1 mV s^{-1}.

Fig. 9. Nyquist plots of macroporous Li[Li$_{0.2}$Mn$_{0.54}$Ni$_{0.13}$Co$_{0.13}$]O$_2$ after (a) 3 cycles and (b) 50 cycles at the charge state of 4.5 V, (c) equivalent circuit performed to fit the curves in (a, b).

and Z_w represent the non-ideal capacitance of the surface layer, non-ideal capacitance of the double-layer and Warburg impedance, respectively. The values of R_e and R_f are similar, between 3 and 7.5 Ω, whenever after 3 cycles or 50 cycles. There is no distinct difference for these oxide electrodes. However, the values of R_{ct} are different, and they are 89.6 Ω, 39.6 Ω and 51.1 Ω for LMNCO-700,

LMNCO-800 and LMNCO-900 after 3 cycles, respectively. LMNCO-800 which owns well-formed layered structure and moderate particle size has the least R_{ct}. Thus, the discharge capacity of LMNCO-800 at the beginning of the cycling is the highest. After cycling at a current density of 200 mA h g^{-1} for 50 cycles, the values of R_{ct} increase distinctly for all the electrodes. 171.2 Ω, 127.3 Ω and 73.4 Ω are obtained for LMNCO-700, LMNCO-800 and LMNCO-900, respectively. LMNCO-900 has the smallest R_{ct} after long cycling, which is accordant with the results obtained in cycle performance. In comparison with the material characterization and electrochemical performances, high crystallinity and hexagonal ordering

are necessary for low value of R_{ct}, then resulting satisfactory rate capability and cyclic stability. Furthermore, small particle size with large specific surface area can effectively improve the rate capability but suffer from more undesirable reactions with the electrolyte, leading to the collapse of the surface structure and poor cyclic stability [10]. In this present work, macroporous structure and good contacts between the active particles contribute a lot to the improved rate capability of LMNCO-900 with large particle size. Meanwhile, small specific surface area of LMNCO-900 makes it possible for stable cycling.

GITT tests are carried out to evaluate Li^+ diffusion in the Li-rich layered oxide after activation for three cycles. Fig. 10a shows the GITT curves of LMNCO-800 and LMNCO-900 during the fourth discharge process between 2.0 V and 4.8 V. The chemical diffusion coefficient of Li^+ (D_{Li+}) is calculated according to Eq. (2) derived by Weppner and Huggins as follows [54]:

$$D_{Li^+} = \frac{4}{\pi}\left(\frac{mV_M}{MA}\right)^2\left(\frac{\Delta E_s}{\tau(dE_\tau/d\sqrt{\tau})}\right)^2\left(\frac{\tau << L^2}{D_{Li^+}}\right) \quad (2)$$

Where V_M is the molar volume of the compound, which is 20.17 and 20.14 cm³ mol⁻¹ for LMNCO-800 and LMNCO-900 deduced from the crystallographic data. M and m are the molecular weight and the mass of $Li[Li_{0.2}Mn_{0.54}Ni_{0.13}Co_{0.13}]O_2$, respectively. A is the interface between the active material and electrolyte, which is based on the result of the BET test. L is the radius of the active particle. Fig. 10b shows a typical t versus E profile for a single titration. If E versus $\tau^{1/2}$ shows a straight line behavior over the

entire period of current flux, as shown in Fig. 10c, Eq. (2) can be further simplified as follows [54,55]

$$D_{Li^+} = \frac{4}{\pi\tau}\left(\frac{mV_M}{MA}\right)^2\left(\frac{\Delta E_s}{\Delta E_\tau}\right)^2 \quad (3)$$

Based on Eq. (3) and GITT measurement, the D_{Li+} at varied voltages during the whole discharge process can be obtained, as shown in Fig. 10d. It increases almost the whole discharge process from 4.5 to 2.5 V. The D_{Li+} values are in the range of 5.0×10^{-18}–8.0×10^{-14} cm² s⁻¹, and no distinct stable region is observed. The absence of a stable region during the whole discharge process may be due to the complex dynamics, which is impossible to be differentiated clearly [46]. It can also be proved from the CV curves: a large and broad cathodic peak almost stretches across the whole discharge process, including a lot of lithium-insertion processes. The reactions during the charge–discharge process are extremely complex, which include not only Li^+ diffusion but also oxygen loss, metal ion dissolution and structural rearrangement. Thus, the D_{Li+} obtained here should be regarded as pseudo or apparent diffusion coefficients. In comparison with typical layered oxides such as $LiCoO_2$ (10^{-7}–10^{-11} cm² s⁻¹) [56] and $LiNi_{1/3}Co_{1/3}Mn_{1/3}O_2$ (10^{-9}–10^{-10} cm² s⁻¹) [57], the D_{Li+} in the Li-rich layered oxide is extremely small. This is understandable because abundant lattice disorders are produced during the transformation from $Li[Li_{0.2}Mn_{0.54}Ni_{0.13}Co_{0.13}]O_2$ to Li_xMO_2. The resultant crystal lattice is not perfect, which therefore retards the Li^+ diffusion. The excellent rate capability in this work is probably attributed to the macroporous structure and good contacts
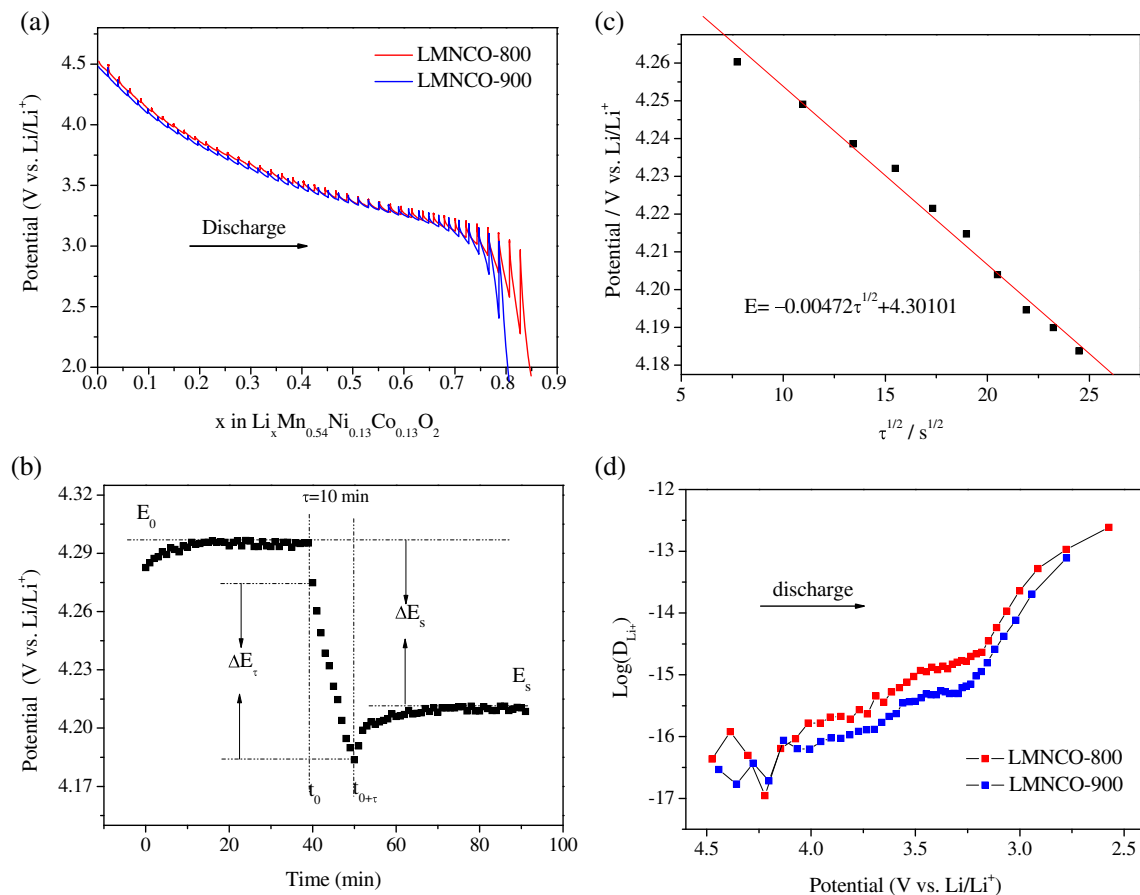
Fig. 10. (a) GITT curves of macroporous $Li[Li_{0.2}Mn_{0.54}Ni_{0.13}Co_{0.13}]O_2$ for the fourth discharge between 2.0 V and 4.8 V (current flux: 40 mA g⁻¹, time interval: 40 min), (b) t vs E profile of $Li[Li_{0.2}Mn_{0.54}Ni_{0.13}Co_{0.13}]O_2$ for a single GITT titration, (c) Linear behavior of E vs $\tau^{1/2}$, (d) diffusion coefficients of Li^+ in $Li[Li_{0.2}Mn_{0.54}Ni_{0.13}Co_{0.13}]O_2$ at different discharge states.

between the active particles obtained by aerogel template, especially for LMNCO-900 which has large particle size. Such design of Li-rich oxide particle morphology will maximize the rate capability benefits and improve the cyclic stability.

4. Conclusions

Macroporous $Li_{1.2}Mn_{0.54}Ni_{0.13}Co_{0.13}O_2$ cathode materials are prepared by aerogel template followed by solid state reaction. The macroporous $Li_{1.2}Mn_{0.54}Ni_{0.13}Co_{0.13}O_2$ with high crystallinity and hexagonal order delivers high discharge capacities at high current densities. The effect of macroporous structure is distinctly revealed through the Li-rich layered oxide synthesized at 900 °C which has large particle size and small specific surface area, but improved rate capability and cyclic stability. EIS and GITT results also indicate that the improved rate capability and cyclic stability are attributed to the contribution of the macroporous structure with good particle contacts. The macroporous $Li[Li_{0.2}Mn_{0.54}Ni_{0.13}Co_{0.13}]O_2$ materials may be promising for large scale application in lithium-ion batteries.

Acknowledgments

References

[1] K.J. Rosina, M. Jiang, D.L. Zeng, E. Salager, A.S. Best, C.P. Grey, J. Mater. Chem. 22 (2012) 20602.
[2] S.J. Shi, J.P. Tu, Y.Y. Tang, Y.Q. Zhang, X.Y. Liu, X.L. Wang, C.D. Gu, J. Power Sources 225 (2013) 338.
[3] J.-H. Park, J.-H. Cho, S.-B. Kim, W.-S. Kim, S.-Y. Lee, S.-Y. Lee, J. Mater. Chem. 22 (2012) 12574.
[4] H.B. Ren, X. Li, Z.H. Peng, Electrochim. Acta 56 (2011) 7088.
[5] S.J. Shi, J.P. Tu, Y.Y. Tang, Y.X. Yu, Y.Q. Zhang, X.L. Wang, C.D. Gu, J. Power Sources 228 (2013) 14.
[6] S.J. Shi, J.P. Tu, Y.J. Mai, Y.Q. Zhang, Y.Y. Tang, X.L. Wang, Electrochim. Acta 83 (2012) 105.
[7] J. Liu, A. Manthiram, J. Mater. Chem. 20 (2010) 3961.
[8] W.C. West, J. Soler, B.V. Ratnakumar, J. Power Sources 204 (2012) 200.
[9] J.H. Kim, M.S. Park, J.H. Song, D.J. Byun, Y.J. Kim, J.S. Kim, J. Alloys Compd. 517 (2012) 20.
[10] J.M. Zheng, X.B. Wu, Y. Yang, Electrochim. Acta 56 (2011) 3071.
[11] S. Kim, C. Kim, Y.-I. Jhon, J.-K. Noh, S.H. Vemuri, R. Smith, K.Y. Chung, M.S. Jhon, B.-W. Cho, J. Mater. Chem. 22 (2012) 25418.
[12] S.J. Shi, J.P. Tu, Y.J. Mai, Y.Q. Zhang, C.D. Gu, X.L. Wang, Electrochim. Acta 63 (2012) 112.
[13] J.L. Liu, L. Chen, M.Y. Hou, F. Wang, R.C. Che, Y.Y. Xia, J. Mater. Chem. 22 (2012) 25380.
[14] C. Yu, G.S. Li, X.F. Guan, J. Zheng, D. Luo, L.P. Li, Phys. Chem. Chem. Phys. 14 (2012) 12368.
[15] Y. Jiang, Z. Yang, W. Luo, X.-L. Hu, W.-X. Zhang, Y.-H. Huang, J. Mater. Chem. 22 (2012) 14964.
[16] J. Liu, B.R. Jayan, A. Manthiram, J. Phys. Chem. C 114 (2010) 9528.
[17] J. Gao, J. Kim, A. Manthiram, Electrochem. Commun. 11 (2009) 84.
[18] J. Liu, Q.Y. Wang, B. Reeja-Jayan, A. Manthiram, Electrochem. Commun. 12 (2010) 750.
[19] J.M. Zheng, Z.R. Zhang, X.B. Wu, Z.X. Dong, Z. Zhu, Y. Yang, J. Electrochem. Soc. 155 (2008) A775.
[20] W. He, J.F. Qian, Y.L. Cao, X.P. Ai, H.X. Yang, RSC Adv. 2 (2012) 3423.
[21] C.J. Jafta, K.I. Ozoemen, M.K. Mathe, W.D. Roos, Electrochim. Acta 85 (2012) 411.
[22] J. Zheng, S.N. Deng, Z.C. Shi, H.J. Xu, H. Xu, Y.F. Deng, Z. Zhang, G.H. Chen, J. Power Sources 221 (2013) 108.
[23] F. Wu, H.Q. Lu, Y.F. Su, N. Li, L.Y. Bao, S. Chen, J. Appl. Electrochem. 40 (2010) 783.
[24] J.H. Lim, H. Bang, K.S. Lee, K. Amine, Y.K. Sun, J. Power Sources 189 (2009) 571.
[25] S.H. Kang, M.M. Thackeray, Electrochem. Commun. 11 (2009) 748.
[26] Q.W. Peng, Z.Y. Tang, L.Q. Zhang, X.J. Liu, Mater. Res. Bull. 44 (2009) 2147.
[27] S. Sivaprakash, S.B. Majumder, Solid State Ionics 181 (2010) 730.
[28] Y.J. Wei, K. Nikolowski, S.Y. Zhan, H. Ehrenberg, S. Oswald, G. Chen, C.Z. Wang, H. Chen, Electrochem. Commun. 11 (2009) 2008.
[29] D. Kim, S.-H. Kang, M. Balasubramanian, C.S. Johnson, Electrochem. Commun. 12 (2010) 1618.
[30] S.J. Shi, J.P. Tu, Y.Y. Tang, Y.X. Yu, Y.Q. Zhang, X.L. Wang, J. Power Sources 221 (2013) 300.
[31] Y.Q. Qiao, J.P. Tu, X.L. Wang, D. Zhang, J.Y. Xiang, Y.J. Mai, C.D. Gu, J. Power Sources 196 (2011) 7715.
[32] Q.Q. Xiong, J.P. Tu, Y. Lu, J. Chen, Y.X. Yu, X.L. Wang, C.D. Gu, J. Mater. Chem. 22 (2012) 18639.
[33] K.M. Shaju, P.G. Bruce, Adv. Mater. 18 (2006) 2330.
[34] N.N. Sinha, N. Munichandraiah, J. Electrochem. Soc. 157 (2010) A647.
[35] Y.Y. Hu, Y.K. Zhou, J. Wang, Z.P. Shao, Mater. Chem. Phys. 129 (2011) 296.
[36] Q. Jiang, Y.L. Xu, C.J. Zhao, X.Z. Qian, S.W. Zheng, J. Solid State Electrochem. 16 (2012) 1503.
[37] M. Mirzaeian, P.J. Hall, Electrochim. Acta 54 (2009) 7444.
[38] F. Zhang, S. Passerini, B.B. Owens, W.H. Smyrl, Electrochem. Solid-State Lett. 4 (2001) A221.
[39] P.E. Tang, J.S. Sakamoto, E. Baudrin, B. Dunn, J. Non-Cryst. Solids 350 (2004) 67.
[40] J.S. Kim, C.S. Johnson, J.T. Vaughey, M.M. Thackeray, S.A. Hackney, W. Yoon, C.P. Grey, Chem. Mater. 16 (2004) 1996.
[41] W.S. Yoon, S. Iannopollo, C.P. Grey, D. Carlier, J. Gorman, J. Reed, G. Ceder, Electrochem. Solid-State Lett. 7 (2004) A167.
[42] S.H. Kang, M.M. Thackeray, C.S. Johnson, J.T. Vaughey, S.A. Hackney, Electrochem. Commun. 8 (2006) 1531.
[43] C.X. Cheng, L. Tan, H.W. Liu, X.T. Huang, Mater. Res. Bull. 46 (2011) 2032.
[44] A.M.A. Hashem, A.E. Abdel-Ghany, A.E. Eid, J. Trottier, K. Zaghib, A. Mauger, C.M. Julien, J. Power Sources 196 (2011) 8632.
[45] M.M. Thackeray, S.H. Kang, C.S. Johnson, J.T. Vaughey, R. Benedek, S.A. Hackney, J. Mater. Chem. 17 (2007) 3053.
[46] C.S. Johnson, N. Li, C. Lefief, J.T. Vaughey, M.M. Thackeray, Chem. Mater. 20 (2008) 6095.
[47] H. Sclar, D. Kovachev, E. Zhechev, R. Stoyanov, R. Lavi, G. Kimmel, J. Grinblat, O. Girshevitz, F. Amalraj, O. Haik, E. Zinigra, B. Markovsky, D. Aurbach, J. Electrochem. Soc. 156 (2009) A938.
[48] A. Ito, D. Li, Y. Sato, M. Arao, M. Watanabe, M. Hatano, H. Horie, Y. Ohsaw, J. Power Sources 195 (2010) 567.
[49] J. Park, J.H. Seo, G. Plett, W. Lu, A.M. Sastry, Electrochem. Solid-State Lett. 14 (2011) A14.
[50] D.H. Jang, Y.J. Shin, S.M. Oh, J. Electrochem. Soc. 143 (1996) 2204.
[51] M. Wohlfahrt-Mehrens, C. Vogler, J. Garche, J. Power Sources 127 (2004) 58.
[52] H.L. Hayley, Y. Naoaki, S.M. Ying, K. Sundeep, B. Julien, P.G. Clare, S.-H. Yang, Chem. Mater. 19 (2007) 2551.
[53] S.K. Hu, G.H. Cheng, M.Y. Cheng, B.J. Hwang, R. Santhanam, J. Power Sources 188 (2009) 564.
[54] W. Weppner, R.A. Huggins, J. Electrochem. Soc. 124 (1977) 1569.
[55] Y.Q. Qiao, J.P. Tu, X.L. Wang, J. Zhang, Y.X. Yu, C.D. Gu, J. Phys. Chem. C 115 (2011) 25508.
[56] M. Park, X.C. Zhang, M. Chung, G.B. Less, A.M. Sastry, J. Power Sources 195 (2010) 7904.
[57] K.M. Shaju, G.V.S. Rao, B.V.R. Chowdariz, J. Electrochem. Soc. 151 (2004) A1324.